ADVANCED ENERGY MATERIALS
www.advenergymat.de

Quantifying and Suppressing Proton Intercalation to Enable High-Voltage Zn-Ion Batteries

Fei Wang, Lauren E. Blanc, Qin Li, Antonio Faraone, Xiao Ji, Huaiyu H. Chen-Mayer, Rick L. Paul, Joseph A. Dura, Enyuan Hu, Kang Xu, Linda F. Nazar,* and Chunsheng Wang**

Rechargeable Zn-ion batteries (ZIBs) are widely regarded as promising candidates for large-scale energy storage applications. Like most multivalent battery systems (based on Zn, Mg, Ca, etc.), further progress in ZIB development relies on the discovery and design of novel cathode hosts capable of reversible Zn^{2+} (de)intercalation. Herein, this work employs VPO_4F as a ZIB cathode and explores ensuing intercalation mechanisms along with interfacial dynamics during cycling to quantify the water dynamics in concentrated electrolytes and/or hybrid aqueous-non aqueous (HANEs) electrolyte(s). Like most oxide-based cathode materials, proton (H^+) intercalation dominates electrochemical activity during discharge of $Zn_xH_yVPO_4F$ in aqueous media due to the hydroxylated nature of the interface. Such H^+ electrochemistry diminishes low-rate and/or long-term electrochemical performance of ZIBs which inhibits implementation for practical applications. Thus, quantification of the water dynamics in various electrolytes is demonstrated for the first time. Detailed investigations of water mobility in various concentrated electrolytes and HANEs systems enable the design of an electrolyte that enhances aqueous anodic stability and suppresses water/proton activity during discharge. Tuning Zn^{2+}/H^+ intercalation kinetics simultaneously allows for a high voltage (1.9 V) and long-lasting aqueous zinc-ion battery: $Zn|Zn(OTf)_2{\cdot}nH_2O\text{-}PC|Zn_xH_yVPO_4F$.

1. Introduction

Wide-spread environmental concerns and the impending energy crisis demand a transition from fossil fuels to renewable resources (e.g., wind, solar), necessitating energy storage to level out their intermittency. Electrochemical energy storage is promising in this respect, as it is dispatchable and can be easily implemented into the grid. Wide-scale commercialization, however, requires energy storage systems beyond options currently available on the market. Despite their excellent performance and high energy density, Li-ion batteries using liquid organic electrolytes are not ideal for large-scale storage due to concerns with their cost, safety, and need for system-level infrastructures such as air-conditioned housing for use in solar energy farms in hot climates. Thus, the demand for affordable, safe batteries is driving the development of new chemistries beyond Li ion.[1–4] Multivalent-ion batteries have garnered considerable attention for potential application in both vehicular and stationary electrochemical storage systems.[5,6] Among them, aqueous rechargeable Zn-ion batteries (ZIBs) are particularly promising owing to their significant cost benefit. The redox potential of Zn (–0.74 V versus SHE) allows for reversible stripping and plating of a metal negative electrode (anode) in aqueous electrolytes, offering excellent conductivity and intrinsic safety.[7] Zn-based technology also benefits from low production costs

F. Wang, Q. Li
Department of Materials Science
Fudan University
Shanghai 200438, China

L. E. Blanc, L. F. Nazar
Department of Chemistry and the Waterloo Institute for Nanotechnology
University of Waterloo
Waterloo, Ontario N2L 3G1, Canada
E-mail: lfnazar@uwaterloo.ca

A. Faraone, H. H. Chen-Mayer, R. L. Paul, J. A. Dura
NIST Center for Neutron Research
National Institute of Standards and Technology
Gaithersburg, MD 20899, USA

The ORCID identification number(s) for the author(s) of this article can be found under https://doi.org/10.1002/aenm.202102016.

X. Ji, C. Wang
Department of Chemical and Biomolecular Engineering
University of Maryland
College Park, MD 20742, USA
E-mail: cswang@umd.edu

E. Hu
Chemistry Division
Brookhaven National Laboratory
Upton, NY 11973, USA

K. Xu
Energy Storage Branch
Energy and Biomaterials Division
Sensor and Electron Devices Directorate
U.S. Army Research Laboratory
Adelphi, MD 20783, USA
E-mail: conrad.k.xu.civ@mail.mil

DOI: 10.1002/aenm.202102016

owing to the ability to manufacture cells in open air environments. Finally, significant progress in ZIB research has offered many solutions to the long-existing detriments of primary alkaline cells, including dendritic zinc deposition and the formation of irreversible byproducts.[8,9]

Despite these advantages, there are several challenges remaining in the development of Zn-ion (and similar multivalent) systems due to the strong Coulombic interactions exhibited by divalent cations: (1) the paucity of positive electrode (cathode) materials capable of fast and reversible intercalation mechanisms,[4,5] and (2) significant desolvation penalties complicating insertion processes at the electrode–electrolyte interface.[10] The wealth of ZIB literature reports the aqueous electrochemistry of materials with open frameworks, such as simple metal oxide cathodes based on Mn or V redox centers (typically 1.3 and 0.8 V versus Zn, respectively) or Prussian blue analogs (PBAs, ≈1.7 V versus Zn).[11–13] Early studies emphasized Mn-based cathode materials, as they are inexpensive and already commercially available in primary cells.[14,15] An alternative to the conversion-based chemistry exhibited by Mn oxides is provided by intercalation cathodes. These efforts were pioneered by the development of $Zn_{0.25}V_2O_5$,[1] and widely extended to layered vanadium oxides stabilized by a variety of pillaring agents.[16–18] This transition from Mn- to V-based cathodes benefits reversibility and cycle life but compromises cell voltage and limits the energy density achievable. PBAs deliver much higher redox potentials, but these materials traditionally suffer from low capacities.[19–21] All the above-mentioned cathodes have large diffusion channels or layer structures, which makes insertion of the hydrated Zn^{2+} highly possible. For ZIBs to compete with existing battery chemistries, cathodes that reversibly deliver both a high voltage and capacity on discharge are needed. Recent reports have demonstrated that promising strategies toward this goal include (1) introducing additional redox couples to PBA frameworks (to increase capacity),[22] or (2) developing polyanionic cathodes (with higher operating voltages relative to oxide materials).[23–26] Like PBAs, modifications to the electronic structure of polyanionic cathodes (e.g., via the substitution/variation of transition metal redox couples and/or anions present) has had positive impact on electrochemical performance in monovalent Li- and Na-ion systems.[27–30] Such nuanced design strategies have not yet been applied to develop polyanionic Zn-ion cathodes, however, since this field is in its infancy (relative to monovalent batteries) and more fundamental issues challenge this progressing technology. Recent reports of hybrid systems have demonstrated impressive electrochemistry of high voltage $VOPO_4$ cathodes in Zn cells using concentrated Zn^{2+}/Li^+ or Zn^{2+}/Na^+ electrolytes.[31,32] These systems offer excellent cycling stability with reversible vanadium and/or oxygen redox mechanisms. However, the high concentration of monovalent cations in the electrolyte can lead to significant competition between Li^+/Na^+ and Zn^{2+} intercalation processes at the positive electrode.

To advance polyanionic cathodes for ZIBs, research must address a critical challenge complicating the electrochemistry of all oxide cathodes in aqueous electrolytes: the competition between Zn^{2+} and proton (H^+) energy storage mechanisms. Water benefits Zn^{2+} insertion by accelerating Zn^{2+} diffusion at the interface and in the cathode lattice.[33–35] However, water also strongly interacts on the hydroxylated interface of an oxide material to promote H^+ intercalation into the cathode.[36] Competition between Zn^{2+} versus H^+ co-intercalation is more likely to favor the latter process when high-voltage polyanionic frameworks are involved that push the anodic stability of water-based electrolytes (e.g., $Na_3V_2(PO_4)_2F_3$),[37] unlike lower voltage oxide materials—such as $V_3O_7 \cdot H_2O$—where Zn^{2+} intercalation precedes the onset of significant proton activity.[10,36] Proton insertion arising from water "splitting" is accompanied by simultaneous deposition of a layered double hydroxide (LDH) comprised of Zn^{2+} and electrolyte/hydroxide anions. This precipitate is often overlooked during ex situ analysis as it is typically washed from the electrode surface prior to characterization. This further complicates interpretation of electrochemical characterization and results in conflicting reports where H^+ insertion was detected in some cases but overlooked in others.[38–42] While proton intercalation offers several advantages over "true" ZIBs and boasts excellent kinetics with impressive cyclability at ultrafast rates, its presence can be problematic. For example, because dissolution of the LDH precipitate is vital to buffer the pH upon H^+ extraction, its physical detachment from the cathode surface prior to charge (which occurs by cycling at low current density and/or pausing before charge) causes irreversible behavior and cell failure.[11,36] For systems to reach viable performance metrics, this challenge must be addressed by either suppressing or balancing proton incorporation while maximizing Zn-ion intercalation at high potential. Thus far, a critical bottle-neck to achieving this goal has been the shortage of methodologies used to quantify proton insertion and measure water mobility in the electrolyte as part of an effort to reduce H^+ electrochemical activity during cycling.

Herein, we demonstrate a high voltage aqueous ZIB enabled by a fluorophosphate cathode (VPO_4F) that achieves a working voltage of ≈1.9 V versus Zn^{2+}/Zn. To quantify the different water dynamics in various media as a function of electrolyte composition, highly concentrated electrolytes and hybrid aqueous/nonaqueous (HANE) electrolytes were characterized and compared using quasi-elastic neutron scattering (QENS).[43,44] Increasing the salt concentration and/or the proportion of nonaqueous solvents successfully suppresses the water dynamics, thus increasing the anodic stability of the electrolyte and promoting Zn^{2+} intercalation at the interface over competing H^+ intercalation and water oxidation processes. The Zn^{2+}/H^+ co-intercalation in HANEs can be successfully regulated using different ratios of aqueous/nonaqueous solvent. In the optimized electrolyte, the VPO_4F cathode exhibits a high energy density of 237 Wh kg^{-1} and high cycling stability with >80% capacity retention after 200 cycles at 0.2 C. This fundamental understanding concerning the interplay of Zn^{2+}/H^+ co-intercalation provides indispensable guidance for the design of aqueous Zn battery systems.

2. Results and Discussions

The crystal structure of monoclinic VPO_4F (**Figure 1**a) consists of a relatively open, corner-sharing network of VO_4F_2 octahedra and PO_4 tetrahedra capable of hosting a variety of guest cations.[45,46] This, along with the presence of an accessible

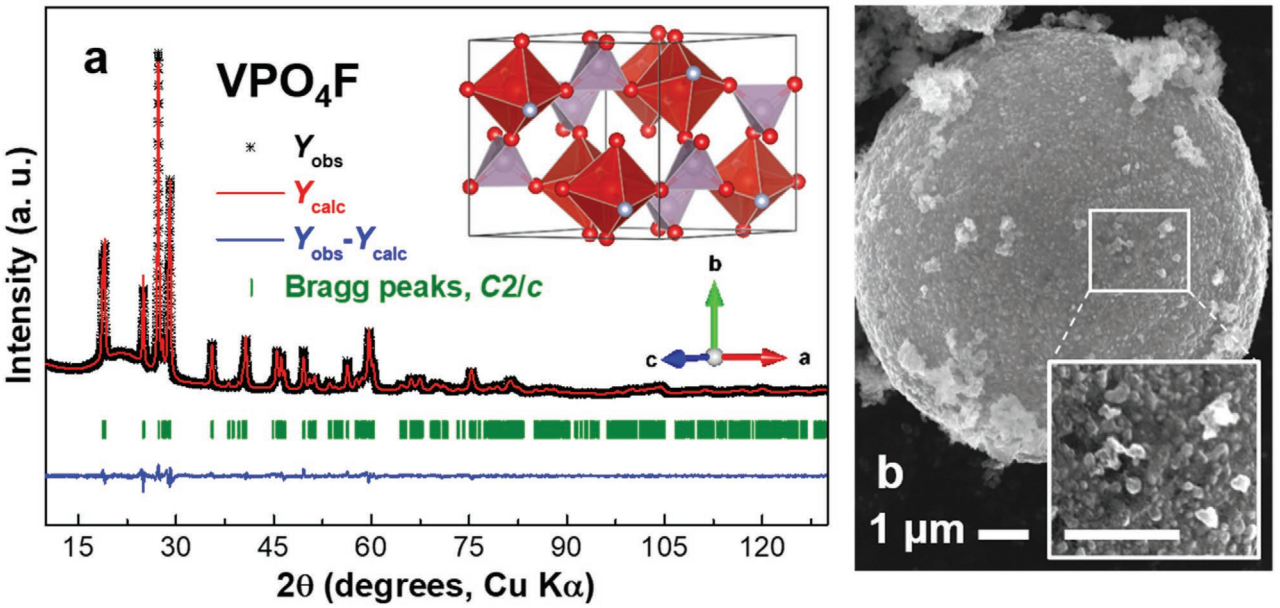

Figure 1. Structure and morphology of the VPO_4F cathode material. a) Rietveld-refined fit of VPO_4F using the monoclinic C2/c space group (no. 15). The inset shows the crystal structure, consisting of VO_4F_2 (red octahedra) and PO_4 (purple tetrahedra). b) Scanning electron microscope (SEM) image of bulk material where the inset magnifies the surface of the aggregate. Both scale bars represent 1 µm.

$V^{4+/3+}$ couple in the lattice renders it an ideal high-voltage (≈2 V) cathode candidate for reversible Zn^{2+} intercalation. Since the VPO_4F active material was prepared through the (electro) chemical oxidation of $LiVPO_4F$,[47] inductively coupled plasma optical emission spectrometry (ICP-OES) was employed to ensure complete delithiation occurred in the oxidized material. The VPO_4F (Figure 1) contained no impurities and the microcrystallites retained the original morphology of the $LiVPO_4F$ precursor (Figure S1, Supporting Information). Rietveld refinement demonstrated that all peaks in the X-ray diffraction (XRD) pattern fit well to the monoclinic space group $C2/c$ (Table S1, Supporting Information). Scanning electron microscope (SEM) analysis revealed that the VPO_4F nanoparticles (≈100 nm) are coated in amorphous carbon and are aggregated into micron-sized (>10 µm) spheres (Figure 1b). This morphology stems from the carbothermal method used to prepare the $LiVPO_4F$ parent powders. The ZIB electrochemistry of VPO_4F was investigated in aqueous media at ambient temperature. Since typical aqueous electrolytes cannot sustain the high-voltage intercalation potential of this fluorophosphate cathode, a concentrated water-in-salt electrolyte was employed to enhance the anodic stability of the aqueous system.

VPO_4F was paired against Zn metal using 4 M $Zn(OTf)_2 \cdot H_2O$ electrolyte, and these cells were discharged at a fairly slow rate (0.2 C) to investigate the distinct electrochemical processes occurring during cycling (**Figure 2**). The presence of several plateaus in Figure 2a indicate that multiple redox transitions occur on discharge. The onset of electrochemical activity begins just below 2 V and the high-voltage process at 1.9 V exhibits a sharp peak, indicative of a two-phase reaction (Figure 2b). The 1.9 V discharge plateau is ascribed to Zn^{2+} insertion into VPO_4F (4.1 V versus Li/Li^+),[48] but this process only accounts for a small portion of the observed capacity (<30%). Below 1.9 V, a sloping discharge profile is observed, with two plateaus which are clearly apparent in the differential capacity (dQ/dV) plot (Figure 2b). The sloping nature suggests that these transitions involve a solid solution-like phase. Such an evolution in electrochemical behavior has been observed in previous studies of oxide cathode materials in aqueous media, and it is typically ascribed to a transition between Zn^{2+} and H^+ electrochemical activity.[23,49] As confirmed below, protons accompany Zn^{2+} insertion into the VPO_4F lattice, yielding a $Zn_xH_yVPO_4F$ material on discharge (Equation 1).

$$xZn^{2+} + yH^+ + (2x+y)e^- + V^{IV}PO_4F \leftrightarrow Zn_xH_yV^{III}PO_4F \quad (1)$$

This reaction has a maximum theoretical capacity of either 136 or 162 mAh g^{-1} (based on the discharged material) depending on whether Zn^{2+} or H^+ cations are the primary charge carriers, respectively. Cation insertion into the VPO_4F lattice relies on the V^{IV}/V^{III} redox couple so that full discharge corresponds to a final composition of $Zn_{0.5-x}H_{2x}VPO_4F$. Due to their high charge density, Zn^{2+}/H^+ are both likely coordinated with H_2O molecule(s) upon insertion at the interface and may yield a hydrated discharge product ($Zn_xH_yVPO_4F \cdot nH_2O$). However, the participation of water is excluded from Equation (1) as solvent/cation co-intercalation should be minimal given that the diameter of a water molecule (≈3 Å) is of the same magnitude as the tunnels in the tavorite framework.[48] As confirmation, thermogravimetric analysis (TGA) was carried out on $Zn_xH_yVPO_4F$ after discharge in the aqueous electrolyte. Analysis of other tunnel structures, such as todorokite, has shown that water bound within the channels is lost at or above 160 °C whereas surface water is lost between 50 °C and 150 °C.[50] In this study, TGA of discharged $Zn_xH_yVPO_4F$ shows mass is lost under 120°C corresponding to the evaporation of water from the surface of the material (Figure S2, Supporting Information). Afterwards, only slight weight lost was detected until

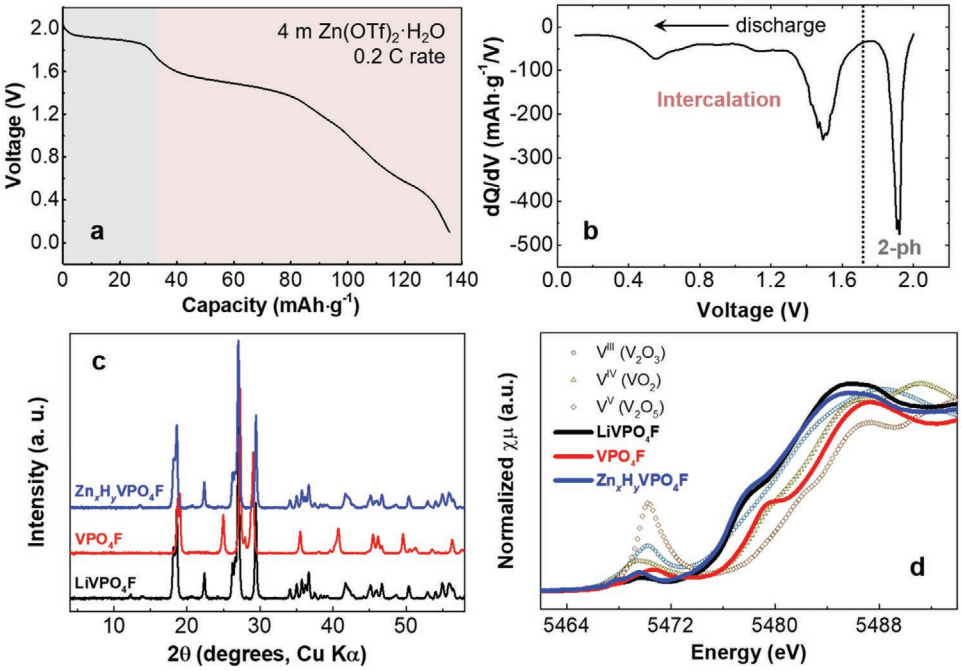

Figure 2. Electrochemical and ex situ characterization of $Zn_xH_yVPO_4F$. a) voltage profile during the first discharge and b) the associated differential capacity curve of VPO_4F in the 4 M $Zn(OTf)_2{\cdot}H_2O$ electrolyte at ambient temperature and 0.2 C rate (1 C: 140 mA g^{-1}; electrode areal mass loading: 10 mg cm^{-2}). Ex situ c) X-ray diffraction (XRD) patterns and d) X-ray absorption near edge structure (XANES) spectra collected at the V K-edge of pristine $LiVPO_4F$ (black), active material VPO_4F (red), and $Zn_xH_yVPO_4F$ discharged to 0.2 V (blue).

380 °C, indicating that no water molecules are present in the tunnels of the structure.

The ex situ XRD patterns of pristine $LiVPO_4F$, delithiated VPO_4F, and discharged $Zn_xH_yVPO_4F$ are shown in Figure 2c. Cation insertion triggers a phase transformation from monoclinic VPO_4F ($C2/c$, no. 15), and the diffraction pattern for $Zn_xH_yVPO_4F$ closely resembles the lithiated tavorite phase ($P\overline{1}$, no. 2). The X-ray absorption near edge structure (XANES) portion of the XAS spectra for lithiated, delithiated, and zincated materials in Figure 2d confirm that V is redox-active during cation ingress/egress and that vanadium is reduced to V (III) on discharge. Zn^{2+} insertion was also unequivocally confirmed by the Zn K-edge XAS data for discharged $Zn_xH_yVPO_4F$, which shows a slight shift to lower binding energy vis a vis $Zn(OTf)_2$ (Figure S3, Supporting Information).

The relative contribution of Zn^{2+} to the total discharge capacity was assessed using a combination of energy dispersive X-ray spectroscopy (EDS) and Rietveld analysis of the XRD pattern (**Figure 3** and Figure S4, Supporting Information). Rietveld refinement of $Zn_xH_yVPO_4F$ reveals that the zincated-protonated material is isostructural with the lithiated tavorite phase (Tables S2 and S3, Supporting Information), and elemental mapping shows Zn^{2+} ions are evenly distributed throughout the VO_4F_2/PO_4 grains (Figure 3c). Unlike $LiVPO_4F$ (but similar to Li_2VPO_4F), [48] $Zn_xH_yVPO_4F$ contains two distinct intercalation sites. The presence of separate Zn^{2+} sites (at low occupancy relative to Li^+) is likely due to the electrostatic repulsion of the divalent cation (Figure S5, Supporting Information). The amount of Zn^{2+} in $Zn_xH_yVPO_4F$ measured by EDS agrees well with the refined Zn^{2+} occupancies determined by Rietveld analysis; however, this composition—$Zn_{0.14}H_yVPO_4F$—only accounts for a fraction of the observed discharge capacity (Table S4, Supporting Information). According to Equation (1), the intercalation of 0.14 Zn^{2+} corresponds to a ≈38 mAh g^{-1} capacity, which suggests that the high voltage (≈1.9 V) discharge plateau observed in Figure 2a corresponds to Zn^{2+} intercalation, and that other electrochemical processes (i.e., H^+ intercalation, capacitive contributions, etc.) account for the capacity observed below 1.9 V. While it is reasonable to expect that proton intercalation accounts for the remaining discharge capacity, XRD characterization cannot quantitatively determine H^+ content, nor its location in the monoclinic lattice. Neutron diffraction is needed to detect protons and fully characterize this phase, and such studies will be the subject of future investigations. In this work, prompt-gamma neutron activation analysis (PGAA) was employed to estimate the relative contribution of proton intercalation to the observed capacity and further explore the electrochemical activity of the aqueous system.

PGAA directly and nondestructively determines the H concentration in materials based on the prompt gamma ray emission resulting from neutron capture by a nucleus. As the emitted gamma rays are characteristic of the capturing nucleus, the PGAA spectrum simultaneously records the multielemental response during irradiation, useful for determining the stochiometric ratios of the matrix elements. To remove water absorbed on the surface of the sample (Figure S2, Supporting Information), the discharged electrode was washed and dried for 72 h at 60°C under vacuum. In dried material, a 4.64 H:Zn ratio in $Zn_xH_yVPO_4F$ was calculated from the PGAA spectrum (with an uncertainty less than 1% based on counting statistics, Figure S6,

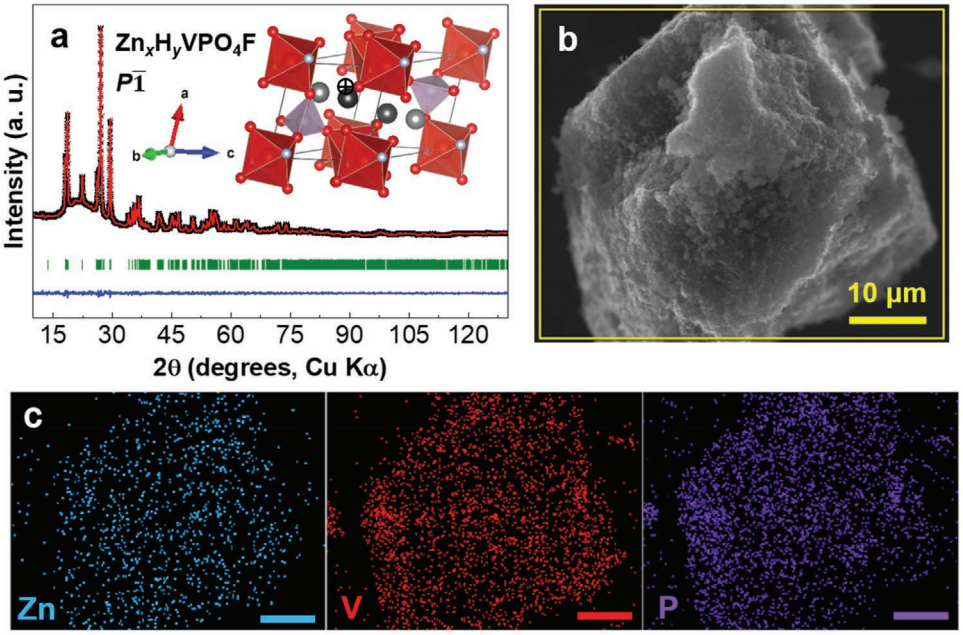

Figure 3. X-ray diffraction (XRD) and scanning electron microscope (SEM) energy dispersive X-ray spectroscopy (EDS) characterization of discharged $Zn_xH_yVPO_4F$. a) Rietveld-refined fit of discharged material showing experimental data (black crosses), fitted data (red line), difference map between observed and calculated data (blue line), and Bragg positions of the triclinic $P\bar{1}$ phase (green ticks). Inset shows the $Zn_xH_yVPO_4F$ crystal structure consisting of intercalated Zn^{2+} (light/dark gray spheres) and H^+ (black circle) within the VO_4F_2/PO_4 lattice (red/purple polyhedra). b) SEM image of discharged $Zn_xH_yPO_4F$ along with c) corresponding elemental mapping of Zn (blue), V (red), and P (purple).

Supporting Information). This analysis suggests that the final composition of discharged material is $Zn_{0.14}H_{0.65}VPO_4F$, so that the high voltage plateau at 1.9 V is properly ascribed to Zn^{2+} insertion, and most of the observed discharge capacity (below 1.7 V) results from H^+ intercalation into the tavorite structure (**Figure 4**a). Following the first discharge, the charge capacity obtained is higher than the initial capacity delivered and corresponds to a relatively low Coulombic efficiency (CE) of 86.4%. At the end of charge, the voltage curve shows a long platform without upward deflection which is characteristic of electrolyte decomposition (Figure 4a). These observations indicate that the 4 M $Zn(OTf)_2 \cdot H_2O$ electrolyte contains "free" (unbound) water molecules that impose undesirable effects on overall performance. Electrolyte decomposition occurs because the electrochemical window of the aqueous electrolyte is still not wide enough to support the high working potential of VPO_4F and (partially) causes the low CE observed in Figure 4b. In addition to the negative impact of electrolyte decomposition, the significant participation of protons in this system may further lead to poor cycling performance at slow rates (0.2 C). Poor (slow rate) cyclability in aqueous media stems from the irreversible nature of the proton dominated intercalation mechanism during discharge, as shown in **Figure 5**.

Thus, the discharge profile of $Zn_xH_yVPO_4F$ in aqueous media is divided into two regions dominated by Zn^{2+} and H^+ intercalation, respectively. At an operating voltage of 1.9 V, Zn^{2+} insertion into the VPO_4F active material triggers a two-phase transition from a monoclinic ($C2/c$) to triclinic ($P\bar{1}$) lattice, similar

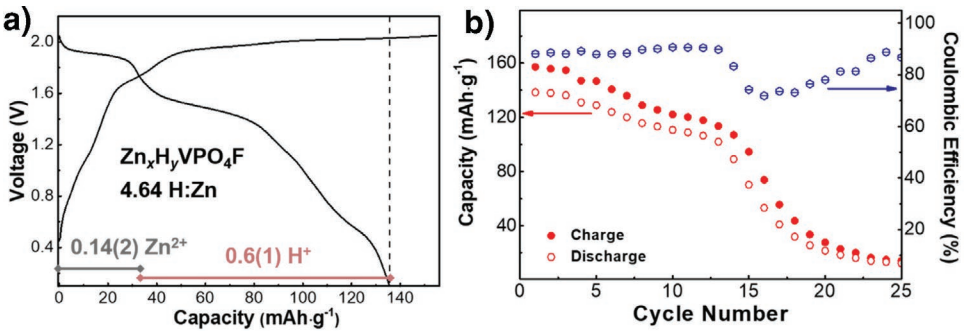

Figure 4. Electrochemistry and cycling performance of $Zn_xH_yVPO_4F$ in aqueous electrolyte. a) The typical voltage profile of VPO_4F between 0.2 and 2.1 V in the 4 M $Zn(OTf)_2 \cdot H_2O$ electrolyte. Inset: H/Zn atom ratio in the discharged VPO_4F electrode. b) The cycling performance of VPO_4F at a relatively slow 0.2 C rate.

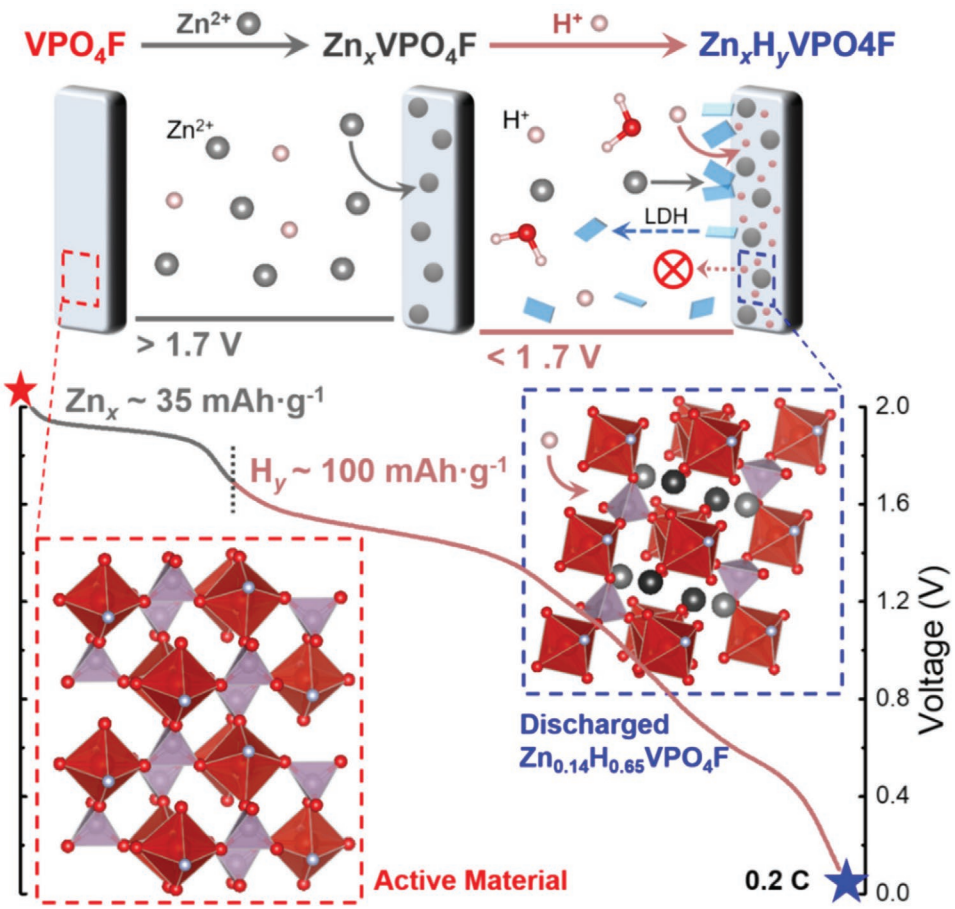

Figure 5. Schematic of Zn^{2+}/H^+ insertion mechanism during discharge of $Zn_xH_yVPO_4F$ in aqueous electrolyte. At high voltage (>1.7 V) Zn^{2+} insertion dominates electrochemical activity, but H^+ intercalation accounts for most of the observed capacity. The latter process exhibits poor reversibility at slow rates as the layered double hydroxide (LDH) precipitate detaches from the cathode surface.

to the electrochemical behavior Li_xVPO_4F.[48,51] After delivering a fairly small capacity (≈35 mAh g^{-1}), Zn^{2+} activity decreases and protons begin to intercalate into the structure to form $Zn_{0.14}H_yVPO_4F$. This process dominates the electrochemistry at potentials below 1.7 V and accounts for most of the total capacity (≈100 mAh g^{-1}). After proton insertion, a locally high gradient of hydroxide anions at the interface is formed where OH^- anions interact with Zn^{2+} and triflate anions to form a LDH precipitate on the electrode surface. The lamellar material exhibits a strong (001) reflection that appears at low angle in XRD patterns during in situ investigations;[36] however the hydroxy-triflate LDH is typically not observed in ex situ characterizations as it is easily washed from the electrode surface during sample preparation. While the LDH is absent from the diffraction pattern of $Zn_xH_yVPO_4F$ that was rigorously washed after discharge (Figure 2c), it can be detected in the diffraction pattern of a gently washed electrode (Figure S7, Supporting Information). Nonetheless, it is evident that this flakey material forms during discharge and easily detaches from the electrode surface during low current density cycling, leading to irreversible behavior and a poor cycle life (≈25 cycles). Thus, the mechanism(s) taking place at high and low voltage (above or below 1.7 V) can best be described by a Zn^{2+} dominated process (Equation 2) or simultaneous H^+/OH^- reactions (Equations 3 and 4), respectively.

$$x\mathrm{Zn}^{2+} + \mathrm{VPO_4F} \leftrightarrow \mathrm{Zn}_x\mathrm{PO_4F} \tag{2}$$

$$y\mathrm{H}^+ + \mathrm{Zn}_x\mathrm{VPO_4F} \leftrightarrow \mathrm{Zn}_x\mathrm{H}_y\mathrm{VPO_4F} \tag{3}$$

$$a\mathrm{Zn}^{2+} + \mathrm{b\ OTf}^- + (2a-b)\mathrm{OH}^- \leftrightarrow \mathrm{Zn}_a(\mathrm{OTf})_b(\mathrm{OH})_{2a-b}\cdot n\mathrm{H_2O} \tag{4}$$

The relative proportion of these two processes depends on the extent of water activity in the electrolyte as well as the reaction kinetics. Equation (2) shows the intercalation mechanism at equilibrium for this ZIB; however, we expect the kinetics of this process to be significantly slower compared to monovalent cation ingress/egress. Thus, while the ultrafast rate performance—along with long-term cyclability at high current densities—of systems reported in the ZIB literature has sparked much intrigue, such desirable metrics are rarely observed in typical multivalent systems. In many aqueous ZIBs, H^+ (de) intercalation is more likely responsible, at least in part, for the observed electrochemistry. However, complications resulting from LDH deposition-dissolution during H^+ (de)intercalation

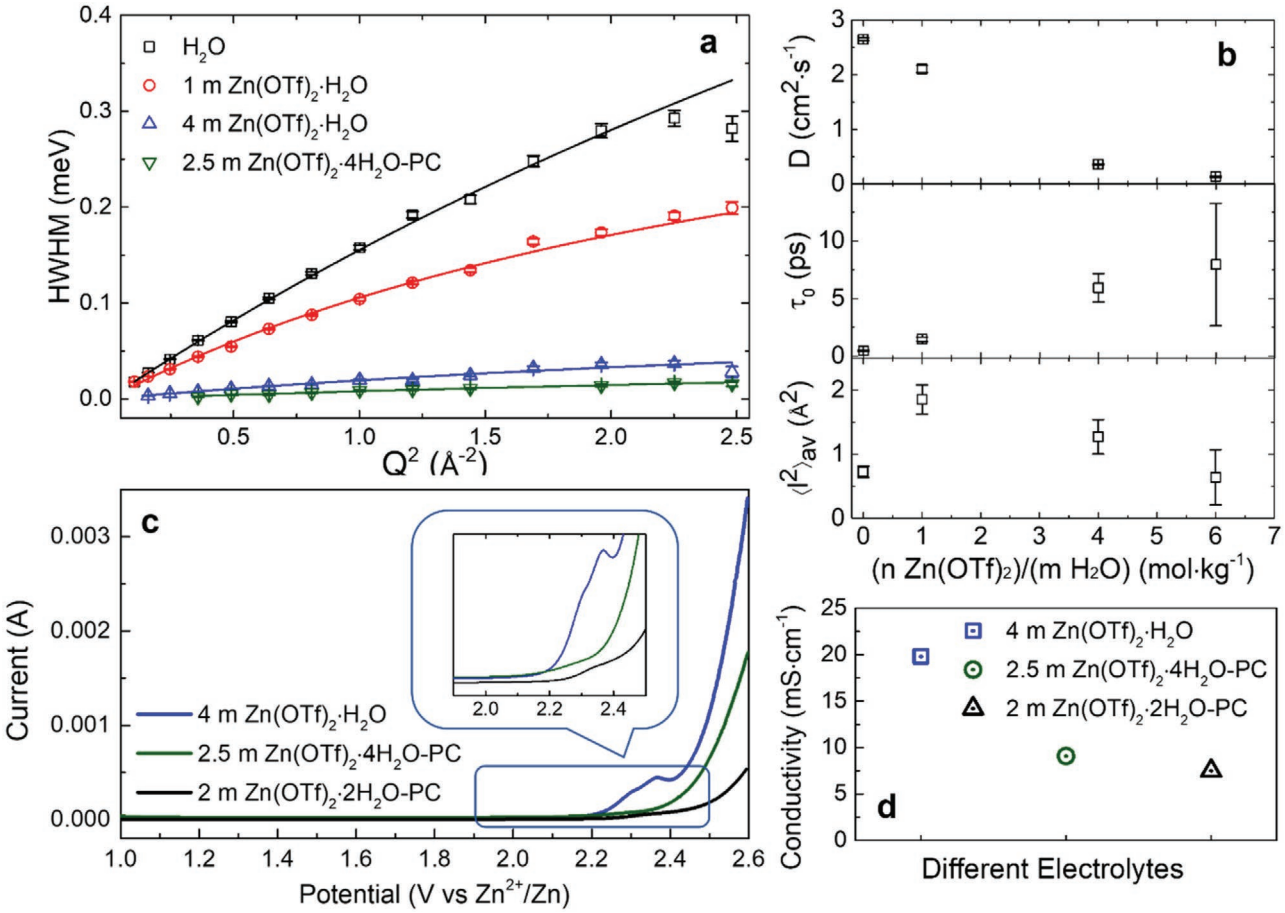

Figure 6. a,b) Quasi-elastic neutron scattering (QENS) analysis of various hybrid aqueous-non aqueous (HANE) systems. The microscopic mobility of water in different electrolytes determined using QENS. Error bars represent one standard deviation. c) The anodic electrochemical stability windows (scan rate: 10 mV s^{-1}) and d) conductivities of different electrolytes.

pose serious impediments. In addition to poor cyclability at low rates (i.e., irreversible H^+ extraction after LDH detachment), in practical applications significant buildup of insulating layers of LDH will increase the impedance across the electrode–electrolyte interface and hinder/halt electrochemical activity. This issue is evidenced by the significant increase of the resistance inside the cell that accompanied the formation of the LDH after discharge (Figure S8, Supporting Information). Therefore, approaches to control Zn^{2+}/H^+ co-intercalation and reduce the water activity are necessary to advance ZIBs as energy storage systems.

To address this problem, we added a nonaqueous solvent into the concentrated electrolytes to increase the electrolyte's stability window and assessed subsequent performance through quantification of the water dynamics in the resulting HANE system. The efficacy of this approach was previously demonstrated in Li-ion systems.[33] In this current work, we use QENS to measure the water mobility in different HANE systems using several dynamic parameters. Owing to the very high incoherent neutron scattering cross-section of hydrogen, QENS measurements yield information on the single particle dynamics of hydrogen atoms in a system over nanoscopic length scales (≈1–10 Å) and timescales (≈1–100 picoseconds). The spectra were analyzed using a common approach in terms of sums of Lorentzian functions (see the Experimental Section in the Supporting Information and Figure S9, Supporting Information). The broadening of the Lorentzian line—usually reported by its half width at half maximum (HWHM) —is inversely proportional to the timescale of the hydrogen atom's motion over a length scale determined by the exchange wavevector, Q. Therefore, a plot of HWHM versus Q^2, can be analyzed according to microscopic models for the motion of the water molecules (Equation 5). In **Figure 6**a the HWHM was fitted using a random jump diffusion model.

$$HWHM = \frac{DQ^2}{1 + DQ^2\tau_0} \tag{5}$$

where D is the self-diffusion coefficient of water and τ_0 is the characteristic time that water molecules remain localized before the next jump occurs. The average mean square jump length is given by $\langle l^2 \rangle_{av} = 6D\tau_0$. In nanoscopically inhomogeneous samples (e.g., ionic liquids), the self-diffusion coefficient determined by this method might differ from the one measured on a macroscopic level using Pulse Gradient Stimulated Echo NMR, but the trends should be consistent. As shown in Figure 6b, the

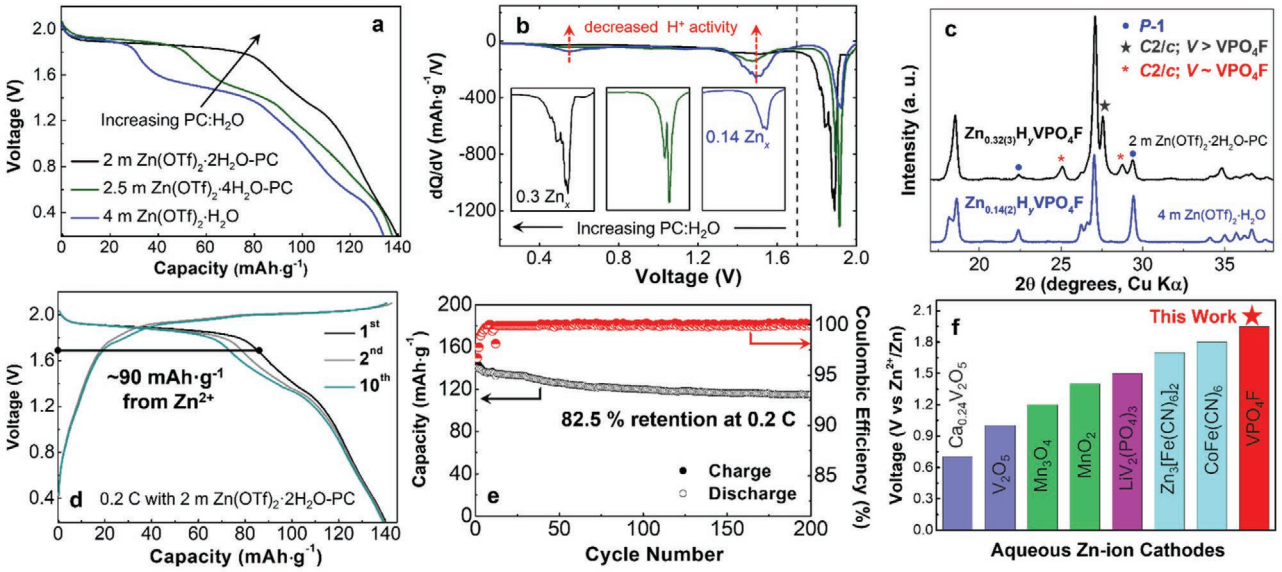

Figure 7. Characterization of $Zn_xH_yVPO_4F$ discharged in hybrid aqueous-non aqueous (HANE) systems. a) The first discharge voltage profile and b) the associated differential capacity curves of $Zn_xH_yVPO_4F$ in different electrolytes at ambient temperature and a 0.2 C rate (1 C: 140 mA g^{-1}, electrode areal mass loading: 10 mg cm^{-2}). For clarity of comparison (a) and (b) share the same legend and the insets of (b) use the same scale. c) Comparison of the X-ray diffraction (XRD) patterns of $Zn_xH_yVPO_4F$ discharged in HANE ($x = 0.32$) versus aqueous ($x = 0.14$) electrolyte. Asterisks mark the three distinct phases identified in $Zn_{0.3}H_yVPO_4F$ after LeBail analysis. The typical d) voltage profile and e) cycling performance of $Zn_xH_yVPO_4$ between 0.2 and 2.1 V in 2 M $Zn(OTf)_2{\cdot}2H_2O$-PC electrolyte. f) Comparison of the working voltage achieved in this work to various reported Zn-ion cathode materials.

data clearly indicate that water mobility slows down as the salt content increases, evidenced by a decrease of the diffusion coefficient and an increase of the residence time. The average jump length, however, exhibits nonmonotonic behavior indicating the complexity of the microscopic dynamics of the water molecules in these electrolytes.

Based on the above guidelines, we prepared a series of $Zn(OTf)_2$ electrolytes with various salt concentrations and H_2O-propylene carbonate (PC) ratios to evaluate their electrochemical window. PC was chosen here for its good stability at high voltages. Figure 6c shows the oxidative stability of different electrolytes measured using cyclic voltammetry (CV) at a scan rate of 10 mV s^{-1}. The addition of a nonaqueous solvent (PC) increases the anodic stability,[52] which is in close agreement with the change in water dynamics. The anodic limits of both 2.5 M $Zn(OTf)_2{\cdot}4H_2O$-PC and 2 M $Zn(OTf)_2{\cdot}2H_2O$-PC electrolytes are higher than 2.2 V, which is sufficient to support the working potential of VPO_4F (1.9 V). Even though the addition of PC decreases the conductivity from 20 mS cm^{-1} for 4 M $Zn(OTf)_2{\cdot}H_2O$ to 8 mS cm^{-1} for 2 M $Zn(OTf)_2{\cdot}2H_2O$-PC (Figure 6d), subsequent electrochemical performance is not significantly affected in the HANE series (**Figure 7**).

As the PC:H_2O ratio increases, the high voltage (≈1.9 V) discharge plateau associated with Zn^{2+} ingress elongates (Figure 7a), demonstrating that not only is water activity suppressed, but simultaneously the Zn^{2+}/H^+ intercalation kinetics are successfully tailored to favor Zn^{2+} insertion (Table S4, Supporting Information). As a result, in 2 M $Zn(OTf)_2{\cdot}2H_2O$-PC electrolyte the $Zn_xH_yVPO_4F$ cathode achieves an energy density of 237 Wh kg^{-1}, which is 30% higher than that obtained in pure aqueous system (4 M $Zn(OTf)_2{\cdot}H_2O$; 182 Wh kg^{-1}). The x value in the fully discharged $Zn_xH_yVPO_4F$ was determined to be ≈0.3 by EDS spectra (Figure S10, Supporting Information). To verify that Zn^{2+} activity truly dominates at high voltage, material was analyzed after partial discharge to 50% state of discharge (SoD) in 2 M $Zn(OTf)_2{\cdot}2H_2O$-PC electrolyte. At this point—near the end of the high-voltage plateau—EDS analysis shows that $Zn_xH_yVPO_4F$ contained a substantial amount of Zn^{2+} ($x = 0.2$), confirming that Zn^{2+} insertion takes place at 1.9 V (Figure S11, Supporting Information). The differential capacity curves of the HANE series demonstrate that the H^+ redox processes observed at low voltages of 1.3 and 0.6 V disappear as the PC:H_2O ratio increases. The insets of Figure 7b show that a single two-phase transition (forming $Zn_{0.14}H_yVPO_4F$) is observed in the 4 M $Zn(OTf)_2{\cdot}H_2O$ electrolyte, but an additional two-phase transition appears in the HANE series to form more deeply zincated $Zn_{0.3}H_yVPO_4F$ material. This behavior closely resembles the Li_xVPO_4F system, where insertion of Li^+ into monoclinic VPO_4F first triggers a structural transformation to form tavorite $LiVPO_4F$. Insertion of additional Li-ions causes a second transformation from the triclinic lattice into a larger monoclinic Li_2VPO_4F phase.[48]

XRD characterization of $Zn_xH_yVPO_4F$ confirms that Zn^{2+} intercalation into VPO_4F triggers similar lattice transformations to those observed in Li_xVPO_4F, but at lower Zn^{2+} occupancies relative to Li^+ cations. Comparison between XRD patterns of $Zn_{0.3}H_yVPO_4F$ and $Zn_{0.14}H_yVPO_4F$ clearly reveals the presence of an additional reflections upon deeper zincation (Figure 7c). The appearance of the new diffraction peak located to the right of the primary reflection (≈28°) suggests the formation of a highly zincated phase, closely resembling the monoclinic Li_2VPO_4F lattice (Figure S12, Supporting Information). However, like the Li_xVPO_4F series, the primary reflections of each of these related phases exhibit significant overlap so that

the structures of these new zincated materials could not be fully resolved given the complexity of the dataset. While Rietveld refinement of the multiphase mixture in $Zn_{0.3}H_yVPO_4F$ is not possible, Le Bail analysis identifies the presence of three distinct phases (Figure S13, Supporting Information). The first phase in $Zn_{0.3}H_yVPO_4F$ closely resembles the triclinic ($P\overline{1}$) phase-pure material obtained after discharge in aqueous electrolyte. Two additional monoclinic phases are present with differing volumes of 382.2(1) Å^3 and 323.8(2) Å^3, respectively (Table S5, Supporting Information). The larger monoclinic phase fits to the same space group ($C2/c$) and exhibits a similar volume compared to Li_2VPO_4F (≈375 Å^3).[48] This behavior indicates that—similar to Li_xVPO_4F electrochemistry—Zn^{2+} insertion first triggers a monoclinic to triclinic phase transformation (from $C2/c$ to $P\overline{1}$) and subsequently causes a second phase transformation back to the original $C2/c$ lattice. While most of the intercalated Zn^{2+} is likely located in this large monoclinic lattice, further investigations are needed to precisely determine this structure and compare it to Li_2VPO_4F. The third phase present in discharged $Zn_{0.3}H_yVPO_4F$ is isostructural with the VPO_4F active material (Table S1, Supporting Information). Since proton intercalation did not cause apparent phase transformation during late stages of discharge in aqueous electrolyte, this smaller monoclinic phase may contain H^+ only within in the VPO_4F lattice. The diffraction pattern of partially discharged (50% SoD) $Zn_{0.2}H_yVPO_4F$ closely resembles that of $Zn_{0.3}H_yPO_4F$, further confirming that Zn^{2+} insertion takes place at high voltage and induces the observed structural transitions (Figure S13, Supporting Information). In addition to residual VPO_4F active material, $Zn_{0.2}H_yVPO_4F$ also contains two additional zincated phases isostructural with—and only slightly smaller than—the $C2/c$ and $P\overline{1}$ phases present after full discharge (Table S6, Supporting Information).

These results demonstrate that incorporating nonaqueous components into ZIB electrolytes benefits electrochemical performance by regulating water activity and influencing the Zn^{2+}/H^+ intercalation dynamics. Using the optimized 2 M $Zn(OTf)_2 \cdot 2H_2O$-PC electrolyte, most of the observed discharge capacity is attributed to Zn^{2+} intercalation which delivers nearly 90 mAh g^{-1} (Figure 7d). Furthermore, the CE of this system stabilizes to ≈100% (Figure 7e), indicating that electrolyte decomposition is nearly eliminated at such low water activity. Cycling at a low rate of 0.2 C exhibits gradual capacity fade; however, the Zn||VPO_4F cell retains of 82.5% of its initial discharge capacity after 200 cycles, confirming that Zn^{2+} intercalation likely dominates the redox process (rather than H^+ insertion and LDH precipitation). This performance is promising relative to well-known Mn- and V-based oxide cathodes that typically report excellent capacity retention for thousands of cycles at fast rates but tend to exhibit poor cyclability (<100 cycles) at slow rates.[11] Comparing these electrochemical results to the redox potentials of selected Zn-ion cathode materials from the literature (Figure 7f), the high working voltage of VPO_4F (1.9 V) is remarkable among the group.[22,23,53–58] Clearly, achieving a high working voltage for an individual cell reduces the need for packaging and the related energy density loss in a serial battery in order to meet the desired voltage for commercialization. The only cathode candidates delivering comparable voltages to this work are PBAs, but their energy density is compromised by much lower capacities.[53] Therefore the VPO_4F electrochemistry in this work offers several distinct advantages over previously reported cathodes for ZIBs. Furthermore, the HANEs approach to tailor Zn^{2+}/H^+ intercalation kinetics in $Zn_xH_yVPO_4F$ could be applied universally to tune the electrochemistry of a wide variety of systems. While large-scale investigations to determine impact on the redox mechanisms of other cathode materials is beyond the scope of the current work, we anticipate that our findings will inspire such studies. In this study, with moderate salt concentration or even a hybrid electrolyte solvent with high PC content, proton intercalation still could not be fully suppressed during discharge. The significant Zn^{2+}/H^+ competition observed here (and frequently in the literature) may raise some further discussion on whether it is suitable to call ZIB systems ZIBs or hybrid ZIBs due to significant participation of monovalent cation(s) in the charge storage mechanism at the positive electrode.

3. Conclusions

Using a combination of analytical techniques, we demonstrate that Zn^{2+}/H^+ co-insertion takes place during discharge of VPO_4F in aqueous electrolytes, where Zn^{2+} inserts into the lattice at a high operating potential of 1.9 V versus Zn in a similar manner to Li^+ electrochemistry and triggers up to two distinct phase transitions (from $C2/c$ to $P\overline{1}$ and then from $P\overline{1}$ to $C2/c$), depending on the degree of zincation. Meanwhile, H^+ co-intercalation appears to exhibit solid-solution behavior. Using PGAA, we were able to differentiate and quantify the contributions from the intercalation of Zn^{2+} and H^+ to the overall capacity of VPO_4F. By employing a hybrid electrolyte, we tailored the electrochemical activity of water, and successfully disfavored H^+ intercalation. In the HANES system, nearly twice as much Zn^{2+} inserts into VPO_4F relative to an aqueous ZIB. When Zn^{2+} dominates electrochemistry, stable cycling is observed at 0.2 C (retaining 82.5% of the original capacity after 200 cycles), and a high energy density of 237 Wh kg^{-1} is attained at high voltage, which—to our best of our knowledge–is the first success of reversible electrochemical insertion/extraction of a divalent ion in the high-voltage VPO_4F tavorite structure. The approach of regulating water activity via hybridizing aqueous and nonaqueous electrolytes components provides a new avenue to modulate electrochemistry of multivalent cations.

4. Experimental Section

Preparation of VPO_4F: VPO_4F was prepared by extraction of Li^+ from commercial $LiVPO_4F$ (Advanced Lithium Electrochemistry (Cayman) Co. Ltd.). The $LiVPO_4F$ precursor was electrochemically charged in a 4 M $Zn(OTf)_2$ electrolyte with Zn as both counter and reference electrodes, with the upper cut-off voltage set at 2.1 V versus Zn. Alternatively, chemical oxidation of $LiVPO_4F$ into VPO_4F was achieved using nitronium tetrafluoroborate (NO_2BF_4) in dry acetonitrile under an Ar atmosphere. Excess NO_2BF_4 was used to ensure complete delithiation of the $LiVPO_4F$. The resulting VPO_4F samples were washed by acetonitrile twice after reaction and dried in a vacuum oven at 80°C for 48 h.

Electrochemical Measurements: Electrodes were fabricated by compressing active materials, carbon black, and polytetrafluoroethylene

(PTFE) at weight ratio of 8:1:1 onto a stainless steel grid. Zinc foil (purity of 99.9% and thickness of 0.1 mm) was used in large excess to avoid capacity decay caused by the anode. The Zn-ion electrolytes were prepared by dissolving zinc trifluoromethanesulfonate ($Zn(OTf)_2$, purchased from TCI) in a mixture of H_2O and/or PC solvent based on the desired molality (mol kg^{-1}). For clarity, the H_2O-PC molar ratio is listed for all hybrid electrolytes. For example, 2.5 M $Zn(OTf)_2{\cdot}4H_2O$-PC indicates that the H_2O-PC molar ratio is 4:1 and the electrolyte was prepared with 2.5 mol $Zn(OTf)_2$ in 1 kg total solvent. In three-electrode cells, VPO_4F was employed as the working, activated carbon as the counter, and Ag/AgCl as the reference electrodes. CV was carried out using a CHI 600E electrochemical work station. Zn/VPO_4F full cells were assembled in CR2032-type coin cells, and galvanostatic (dis)charge experiments were performed on a Land BT2000 battery test system (Wuhan, China) at room temperature.

Material Characterization: XRD measurements were performed on a PANalytical Empyrean diffractometer with Cu Kα radiation ($\lambda = 1.5418$ Å) in Debye–Scherrer geometry. Samples were sealed in a 0.3 mm capillary and X-ray data were collected from 3.2° to 140° (2θ) at a step size of 0.013°. Rietveld refinement[59] was performed by sequentially refining scale factor, zero point, background, lattice parameters, fractional coordinates, occupancies, and atomic displacement parameters using the FullProf suite. Full details of refinement results are presented in Tables S1–S3 (Supporting Information). Material morphologies and elemental compositions were examined using a Zeiss field emission SEM equipped with an EDS detector. Scans were collected at an accelerating voltage of 20 keV.

X-ray absorption spectroscopy (XAS) experiments were carried out at the 7-BM (QAS) beamline of NSLS II, Brookhaven National Laboratory. Data were collected in transmission mode using a Si (111) double-crystal monochromator detuned to 45–55% of its original maximum intensity to eliminate the high-order harmonics. Helium-filled tubes were placed before and after the sample to minimize air absorption. A reference spectrum of V foil was simultaneously collected for energy calibration by using the first inflection point as the K-edge. The XAS data were normalized using the ATHENA software package.[60]

PGAA was carried out at the Cold Neutron PGAA instrument at neutron guide D (NGD) at the NCNR. The H to Zn ratio was obtained by data reduction based on standards and/or gamma ray cross-section and detector efficiency.

QENS measurements were performed on the Disk Chopper Spectrometer (DCS) at the NIST Center for Neutron Research.[1] Further details on the QENS technique, experimental details, and full detail of fitting results (Tables S7–S10, Supporting Information) are reported in the Supporting Information.

Supporting Information

Supporting Information is available from the Wiley Online Library or from the author.

Acknowledgements

F.W. and L.E.B. contributed equally to this work. This research used resources 7-BM (QAS) of the National Synchrotron Light Source II, a DOE Office of Science user facility operated by Brookhaven National Laboratory. Certain commercial equipment, instruments, materials, suppliers, or software were identified in this paper to foster understanding. Such identification does not imply recommendation or endorsement by the National Institute of Standards and Technology, nor does it imply that the materials or equipment identified are necessarily the best available for the purpose. This work was supported by the U.S. Department of Energy (DOE) through ARPA-E grant DEAR0000389 (X.J., and C.W.) and the Joint Center for Energy Storage Research, an Energy Innovation Hub funded by the DOE, Office of Science, Basic Energy Sciences (L.E.B., K.X., and L.F.N.). NSERC is acknowledged by L.F.N. for a Canada Research Chairs, and support through the NSERC Discovery Grant program. E.H. is supported by the Assistant Secretary for Energy Efficiency and Renewable Energy, Vehicle Technology Office of the DOE through the Advanced Battery Materials Research (BMR) Program, including the Battery500 Consortium (contract no. DE-SC0012704).

Conflict of Interest

The authors declare no conflict of interest.

Data Availability Statement

Research data are not shared.

Keywords

aqueous batteries, electrolytes, proton intercalation, Zn-ion batteries

Received: July 1, 2021
Revised: September 3, 2021
Published online:

[1] D. Kundu, B. D. Adams, V. Duffort, S. H. Vajargah, L. F. Nazar, *Nat. Energy* **2016**, *1*, 16119.
[2] S. Chu, Y.i Cui, N. Liu, *Nat. Mater.* **2017**, *16*, 16.
[3] P. Canepa, G. Sai Gautam, D. C. Hannah, R. Malik, M. Liu, K. G. Gallagher, K. A. Persson, G. Ceder, *Chem. Rev.* **2017**, *117*, 4287.
[4] M. Li, J. Lu, X. Ji, Y. Li, Y. Shao, Z. Chen, C. Zhong, K. Amine, *Nat. Rev. Mater.* **2020**, *5*, 276.
[5] X. Sun, V. Duffort, B. L. Mehdi, N. D. Browning, L. F. Nazar, *Chem. Mater.* **2016**, *28*, 534.
[6] A. Ponrouch, C. Frontera, F. Bardé, M. R. Palacín, *Nat. Mater.* **2016**, *15*, 169.
[7] R. Demir-Cakan, M. R. Palacin, L. Croguennec, *J. Mater. Chem. A* **2019**, *7*, 20519.
[8] F. Wang, O. Borodin, T. Gao, X. Fan, W. Sun, F. Han, A. Faraone, J. A. Dura, K. Xu, C. Wang, *Nat. Mater.* **2018**, *17*, 543.
[9] H. Pan, Y. Shao, P. Yan, Y. Cheng, K. S. Han, Z. Nie, C. Wang, J. Yang, X. Li, P. Bhattacharya, K. T. Mueller, J. Liu, *Nat. Energy* **2016**, *1*, 16039.
[10] D. Kundu, S. Hosseini Vajargah, L. Wan, B. Adams, D. Prendergast, L. F. Nazar, *Energy Environ. Sci.* **2018**, *11*, 881.
[11] L. E. Blanc, D. Kundu, L. F. Nazar, *Joule* **2020**, *4*, 771.
[12] B. Tang, L. Shan, S. Liang, J. Zhou, *Energy Environ. Sci.* **2019**, *12*, 3288.
[13] A. Konarov, N. Voronina, J. H. Jo, Z. Bakenov, Y.-K. Sun, S.-T. Myung, *ACS Energy Lett.* **2018**, *3*, 2620.
[14] C. Xu, B. Li, H. Du, F. Kang, *Angew. Chem., Int. Ed.* **2012**, *51*, 933.
[15] N. Zhang, F. Cheng, Y. Liu, Q. Zhao, K. Lei, C. Chen, X. Liu, J. Chen, *J. Am. Chem. Soc.* **2016**, *138*, 12894.
[16] F. Ming, H. Liang, Y. Lei, S. Kandambeth, M. Eddaoudi, H. N. Alshareef, *ACS Energy Lett.* **2018**, *3*, 2602.
[17] X. Chuan, G. Jing, L. Peng, Z. Xixiang, N. Alshareef Husam, *Angew. Chem., Int. Ed.* **2018**, *57*, 3943.
[18] S. Islam, M. H. Alfaruqi, B. Sambandam, D. Y. Putro, S. Kim, J. Jo, S. Kim, V. Mathew, J. Kim, *Chem. Commun.* **2019**, *55*, 3793.
[19] M. Pasta, C. D. Wessells, N. Liu, J. Nelson, M. T. Mcdowell, R. A. Huggins, M. F. Toney, Y.i Cui, *Nat. Commun.* **2014**, *5*, 3007.
[20] R. Y. Wang, B. Shyam, K. H. Stone, J. N. Weker, M. Pasta, H.-W. Lee, M. F. Toney, Y. Cui, *Adv. Energy Mater.* **2015**, *5*, 1401869.
[21] K. Hurlbutt, S. Wheeler, I. Capone, M. Pasta, *Joule* **2018**, *2*, 1950.

[22] L. Ma, S. Chen, C. Long, X. Li, Y. Zhao, Z. Liu, Z. Huang, B. Dong, J. A. Zapien, C. Zhi, *Adv. Energy Mater.* **2019**, *9*, 1902446.
[23] F. Wang, E. Hu, W. Sun, T. Gao, X. Ji, X. Fan, F. Han, X.-Q. Yang, K. Xu, C. Wang, *Energy Environ. Sci.* **2018**, *11*, 3168.
[24] P. Hu, T. Zhu, X. Wang, X. Zhou, X. Wei, X. Yao, W. Luo, C. Shi, K. A. Owusu, L. Zhou, L. Mai, *Nano Energy* **2019**, *58*, 492.
[25] H.-Y. Shi, Y. Song, Z. Qin, C. Li, D.i Guo, X.-X. Liu, X. Sun, *Angew. Chem., Int. Ed.* **2019**, *58*, 16057.
[26] J. S. Ko, P. P. Paul, G. Wan, N. Seitzman, R. H. Deblock, B. S. Dunn, M. F. Toney, J. Nelson Weker, *Chem. Mater.* **2020**, *32*, 3028.
[27] S.-C. Yin, H. Grondey, P. Strobel, M. Anne, L. F. Nazar, *J. Am. Chem. Soc.* **2003**, *125*, 10402.
[28] E. Boivin, R. David, J.-N. Chotard, T. Bamine, A. Iadecola, L. Bourgeois, E. Suard, F. Fauth, D. Carlier, C. Masquelier, L. Croguennec, *Chem. Mater.* **2018**, *30*, 5682.
[29] H. Gao, I. D. Seymour, S. Xin, L. Xue, G. Henkelman, J. B. Goodenough, *J. Am. Chem. Soc.* **2018**, *140*, 18192.
[30] J. Wang, Y. Wang, D.-H. Seo, T. Shi, S. Chen, Y. Tian, H. Kim, G. Ceder, *Adv. Energy Mater.* **2020**, *10*, 1903968.
[31] F. Wan, Y. Zhang, L. Zhang, D. Liu, C. Wang, L.i Song, Z. Niu, J. Chen, *Angew. Chem., Int. Ed.* **2019**, *58*, 7062.
[32] H.-Y. Shi, W. Wu, X. Yang, Z. Jia, Z. Lin, Z. Qin, Y. Song, D. Guo, X. Sun, *J. Power Sources* **2021**, *507*, 230270.
[33] J. Shin, D. S. Choi, H. J. Lee, Y. Jung, J. W. Choi, *Adv. Energy Mater.* **2019**, *9*, 1900083.
[34] F. Wang, W. Sun, Z. Shadike, E. Hu, X. Ji, T. Gao, X.- Q. Yang, K. Xu, C. Wang, *Angew. Chem., Int. Ed.* **2018**, *57*, 11978.
[35] G. Sai Gautam, P. Canepa, W. D. Richards, R. Malik, G. Ceder, *Nano Lett.* **2016**, *16*, 2426.
[36] P. Oberholzer, E. Tervoort, A. Bouzid, A. Pasquarello, D. Kundu, *ACS Appl. Mater. Interfaces* **2019**, *11*, 674.
[37] M. J. Park, A. Manthiram, *ACS Appl. Energy Mater.* **2020**.
[38] W. Sun, F. Wang, S. Hou, C. Yang, X. Fan, Z. Ma, T. Gao, F. Han, R. Hu, M. Zhu, C. Wang, *J. Am. Chem. Soc.* **2017**, *139*, 9775.
[39] F. Wan, L. Zhang, X.i Dai, X. Wang, Z. Niu, J. Chen, *Nat. Commun.* **2018**, *9*, 1656.
[40] W. Liu, L. Dong, B. Jiang, Y. Huang, X. Wang, C. Xu, Z. Kang, J. Mou, F. Kang, *Electrochim. Acta* **2019**, *320*, 134565.
[41] Z. Guo, J. Huang, X. Dong, Y. Xia, L. Yan, Z. Wang, Y. Wang, *Nat. Commun.* **2020**, *11*, 959.
[42] X. Gao, H. Wu, W. Li, Y. Tian, Y. Zhang, H. Wu, L. Yang, G. Zou, H. Hou, X. Ji, *Small* **2020**, *16*, 1905842.
[43] F. Wang, O. Borodin, M. S. Ding, M. Gobet, J. Vatamanu, X. Fan, T. Gao, N. Eidson, Y. Liang, W. Sun, S. Greenbaum, K. Xu, C. Wang, *Joule* **2018**, *2*, 927.
[44] A. Naveed, H. Yang, Y. Shao, J. Yang, N. Yanna, J. Liu, S. Shi, L. Zhang, A. Ye, B. He, J. Wang, *Adv. Mater.* **2019**, *31*, 1900668.
[45] H. Kim, Y. Ishado, Y. Tian, G. Ceder, *Adv. Funct. Mater.* **2019**, *29*, 1902392.
[46] H. Kim, D.-H. Seo, M. Bianchini, R. J. Clément, H. Kim, J. C. Kim, Y. Tian, T. Shi, W.-S. Yoon, G. Ceder, *Adv. Energy Mater.* **2018**, *8*, 1801591.
[47] G. He, W. H. Kan, A. Manthiram, *Chem. Commun.* **2018**, *54*, 13224.
[48] B. L. Ellis, T. N. Ramesh, L. J. M. Davis, G. R. Goward, L. F. Nazar, *Chem. Mater.* **2011**, *23*, 5138.
[49] L. E. Blanc, D. Kundu, L. F. Nazar, *Joule* **2020**, 771.
[50] Y.-F. Shen, S. L. Suib, C.-L. O'young, *J. Am. Chem. Soc.* **1994**, *116*, 11020.
[51] J.-M. Ateba Mba, C. Masquelier, E. Suard, L. Croguennec, *Chem. Mater.* **2012**, *24*, 1223.
[52] S.-D. Han, N. N. Rajput, X. Qu, B. Pan, M. He, M. S. Ferrandon, C. Liao, K. A. Persson, A. K. Burrell, *ACS Appl. Mater. Interfaces* **2016**, *8*, 3021.
[53] L. Ma, N.a Li, C. Long, B. Dong, D. Fang, Z. Liu, Y. Zhao, X. Li, J. Fan, S. Chen, S. Zhang, C. Zhi, *Adv. Funct. Mater.* **2019**, *29*, 1906142.
[54] P. Senguttuvan, S.-D. Han, S. Kim, A. L. Lipson, S. Tepavcevic, T. T. Fister, I. D. Bloom, A. K. Burrell, C. S. Johnson, *Adv. Energy Mater.* **2016**, *6*, 1600826.
[55] N. Zhang, F. Cheng, J. Liu, L. Wang, X. Long, X. Liu, F. Li, J. Chen, *Nat. Commun.* **2017**, *8*, 405.
[56] J. Hao, J. Mou, J. Zhang, L. Dong, W. Liu, C. Xu, F. Kang, *Electrochim. Acta* **2018**, *259*, 170.
[57] J. P. Tafur, J. Abad, E. Román, A. J. Fernández Romero, *Electrochem. Commun.* **2015**, *60*, 190.
[58] L. Zhang, L. Chen, X. Zhou, Z. Liu, *Adv. Energy Mater.* **2015**, *5*, 1400930.
[59] H. M. Rietveld, *J. Appl. Crystallogr.* **1969**, *2*, 65.
[60] B. Ravel, M. Newville, *J. Synchrotron Radiat.* **2005**, *12*, 537.